



Delft University of Technology

Design guidelines for axial turbines operating with non-ideal compressible flows

Giuffre, Andrea; Pini, Matteo

DOI

[10.1115/1.4049137](https://doi.org/10.1115/1.4049137)

Publication date

2021

Document Version

Final published version

Published in

Journal of Engineering for Gas Turbines and Power

Citation (APA)

Giuffre, A., & Pini, M. (2021). Design guidelines for axial turbines operating with non-ideal compressible flows. *Journal of Engineering for Gas Turbines and Power*, 143(1), Article 011004.
<https://doi.org/10.1115/1.4049137>

Important note

To cite this publication, please use the final published version (if applicable).
Please check the document version above.

Copyright

Other than for strictly personal use, it is not permitted to download, forward or distribute the text or part of it, without the consent of the author(s) and/or copyright holder(s), unless the work is under an open content license such as Creative Commons.

Takedown policy

Please contact us and provide details if you believe this document breaches copyrights.
We will remove access to the work immediately and investigate your claim.

Green Open Access added to TU Delft Institutional Repository

'You share, we take care!' - Taverne project

<https://www.openaccess.nl/en/you-share-we-take-care>

Otherwise as indicated in the copyright section: the publisher is the copyright holder of this work and the author uses the Dutch legislation to make this work public.

Design Guidelines for Axial Turbines Operating With Non-Ideal Compressible Flows

Andrea Giuffre'

Propulsion and Power Faculty of
Aerospace Engineering,
Delft University of Technology,
Delft 2629HS, The Netherlands
e-mail: a.giuffre@tudelft.nl

Matteo Pini

Propulsion and Power Faculty of
Aerospace Engineering,
Delft University of Technology,
Delft 2629HS, The Netherlands
e-mail: m.pini@tudelft.nl

The impact of non-ideal compressible flows on the fluid-dynamic design of axial turbine stages is examined. First, the classical similarity equation (CSE) is revised and extended to account for the effect of flow non-ideality. Then, the influence of the most relevant design parameters is investigated through the application of a dimensionless turbine stage model embedding a first-principles loss model. The results show that compressibility effects induced by the fluid molecular complexity and the stage volumetric flow ratio produce an offset in the efficiency trends and in the optimal stage layout. Furthermore, flow non-ideality can lead to either an increase or a decrease of stage efficiency up to 3–4% relative to turbines designed to operate in dilute gas state. This effect can be predicted at preliminary design phase through the evaluation of the isentropic pressure–volume exponent. Three-dimensional (3D) RANS simulations of selected test cases corroborate the trends predicted with the reduced-order turbine stage model. URANS computations provide equivalent trends, except for case study niMM₁, featuring a non-monotonic variation of the generalized isentropic exponent. For such turbine stage, the efficiency is predicted to be higher than the one computed with any steady-state model based on the control volume approach. [DOI: 10.1115/1.4049137]

1 Introduction

Design guidelines based on scaling analysis and synthesized in the form of efficiency maps as function of work and flow coefficient are essential to obtain a preliminary estimate of the size, the shape of the velocity triangles, and the fluid-dynamic performance of turbomachinery stages [1]. While maps for the preliminary design of steam and gas turbines are readily available and their accuracy has been improved over time [2], design criteria for unconventional turbomachinery, i.e., turbomachines operating with flows departing from ideal gas state, are yet to be established. Examples of unconventional turbomachines are turbines for organic Rankine cycle (ORC) power systems [3], turbines for the oil and gas industry operating with heavy fluid molecules, supercritical CO₂ (sCO₂) compressors [4], and high-speed compressors for refrigeration and air-conditioning systems.

In these machines, the occurrence of strong thermo-physical fluid property gradients [5], compressibility, and non-ideal flow effects [6] along the expansion or the compression process arguably alters the share of dissipation induced by the various loss mechanisms, i.e., viscous friction, shocks, and mixing, as compared to standard gas turbines. This may eventually result in optimal designs significantly differing from those that would be attained through the application of existing best practices [1].

Attempts to devise design charts for unconventional turbines can be found in Refs. [7–9]. However, the existing body of work solely relies on semi-empirical loss correlations to predict the stage performance and lack of a thorough validation of results by means of high-fidelity models or experimental data. The adoption of such loss models is debatable in the context of non-ideal compressible fluid dynamics (NICFD), where the flow characteristics in the blade passages can considerably depart from those considered when deriving and calibrating the existing semi-empirical loss correlations. Recent studies [10] pointed out that an adequate physical interpretation of loss mechanisms in ORC turbines and an accurate loss accounting is arguably possible only by resorting to computational fluid-dynamic (CFD) calculations. These,

however, are machine-specific and their use would be excessively demanding for comprehensive investigations targeting the conception of design guidelines.

This work aims at addressing this knowledge gap by means of a theoretical and numerical framework suited to unconventional turbomachinery. The framework encompasses a reduced-order turbine stage model based on classical similarity parameters, e.g., the duty coefficients, and on dimensionless quantities suited to unconventional turbomachinery, namely, the volumetric flow ratio [7] and the isentropic pressure–volume exponent [11], and a validation procedure based on high-fidelity CFD. The fluid-dynamic losses are calculated through a loss model [12,13] derived from first-principles and extended to arbitrary thermo-physical fluid models [14]. The model is used to compute efficiency maps for axial turbines operating with siloxane MM and CO₂ at different volumetric flow ratios in the ideal and non-ideal thermodynamic regime. The selection of these working fluids is dictated by their increasing molecular complexity as compared to air, see Table 1, and by their relevance for industrial applications, i.e., organic Rankine cycle engines [3] and sCO₂ power systems [15]. Herein, the molecular complexity of a fluid is evaluated as the number of active degrees-of-freedom at its critical temperature, as suggested in Ref. [6].

Table 1 Ideal and generalized isentropic exponents for fluids with increasing molecular weight and complexity

Fluid	M/M_{Air}	N	γ_{∞}	$\gamma_{Pv,\min}$
H ₂	0.07	3.0	1.67	1.63
Air	1.00	5.0	1.40	1.44
CO ₂	1.52	7.0	1.29	0.86
R134a	3.52	21.6	1.09	0.81
MM	5.61	77.4	1.03	0.39
D ₆	15.36	211.7	1.01	0.23

The heat capacity ratio is computed in dilute gas state; the minimum value assumed by γ_{Pv} is evaluated in the thermodynamic region defined by $s > 1.01s_c$ and by the thermal stability limits of each molecule.

Manuscript received September 26, 2020; final manuscript received October 22, 2020; published online December 23, 2020. Editor: Jerzy T. Sawicki.

$$N = \frac{2Mc_{v,id}(T_c)}{R} \quad (1)$$

The results are eventually validated by means of three-dimensional (3D) RANS and URANS computations on stage geometries reconstructed to ensure full similarity with the correspondent dimensionless parameters used in the reduced-order model. The specific objectives of the work are (i) to draw design guidelines and fluid-dynamic design maps valid for unconventional axial turbines, (ii) to investigate potential design limits, (iii) to gain insight of the relative share of the various loss mechanisms in such turbine stages, and (iv) to provide physical understanding on the impact of fluid molecule and associated non-ideal flow effects on the efficiency of axial turbine stages. The structure of the paper is as follows. The technical approach is presented first. Next, the results are analyzed and discussed. Finally, concluding remarks summarize the lessons learnt and give a perspective on future work.

2 Methodology

2.1 Scaling Analysis for Unconventional Axial Turbines.

In classical similarity analysis, the efficiency of an axial turbomachinery stage is expressed as

$$\eta = f(\lambda, \phi, \chi, \text{Re}, \text{Ma}, \sigma) \quad (2)$$

where the vector σ represents the stage dimensionless geometrical characteristics (e.g., blade solidity, aspect ratio, etc.) and the fluid properties are usually assumed to be modeled with the perfect gas law. Equation (2) hereinafter will be referred to as classical similarity equation (CSE). In the typical design process of gas turbine stages, the cascade Mach numbers are evaluated once the velocity triangles and stage velocities are computed [16]. The design is then iteratively adjusted to attain stage layouts, which can comply with admissible mechanical and operational constraints. The same procedure can be adopted to design unconventional turbine stages, but at the expense of overlooking the characteristic Mach numbers. As an illustrative example, consider a turbine stage operating with a complex fluid molecule. These stages are characterized by low values of specific work, but may exhibit volumetric flow ratios largely exceeding those of gas turbine stages. This is essentially due to the low heat capacity ratio and high molecular weight of complex working fluids. The normalized isentropic specific work of a turbine stage, which can be written as

$$\psi_w = \frac{\Delta h_{is}}{R_{ref}^* \cdot T_{tref}} = \frac{R^*}{R_{ref}^*} \frac{\gamma}{\gamma - 1} (1 - \alpha^{1-\gamma}) \quad (3)$$

where $R_{ref}^* = 287.06$ is depicted in Fig. 1. The trends show that the normalized work reduces while increasing the fluid molecular complexity and is mildly affected by a change in $\alpha = \rho_{t,0}/\rho_3$ for highly complex fluid molecules. In other words, stage compressibility effects, ascribed here to variations of the stage volumetric flow ratio, can be drastically enhanced—or mitigated—by slightly varying its prescribed specific work. Such effect is not only related to the type of fluid molecule, but also to the thermodynamic regime of the fluid. This influence can be conveniently predicted through the evaluation of the isentropic pressure–volume exponent, i.e., the thermodynamic property allowing one to cast the isentropic pressure–volume relation in the general form $Pv^{\gamma_{Pv}} = K$, as documented in Ref. [11].

$$\gamma_{Pv} = -\left. \frac{v}{P} \frac{\partial P}{\partial v} \right|_s = -\left. \frac{v}{P} \frac{c_p}{c_v} \frac{\partial P}{\partial v} \right|_T \quad (4)$$

This state variable can be related to the fundamental derivative of gas dynamics [17] as follows:

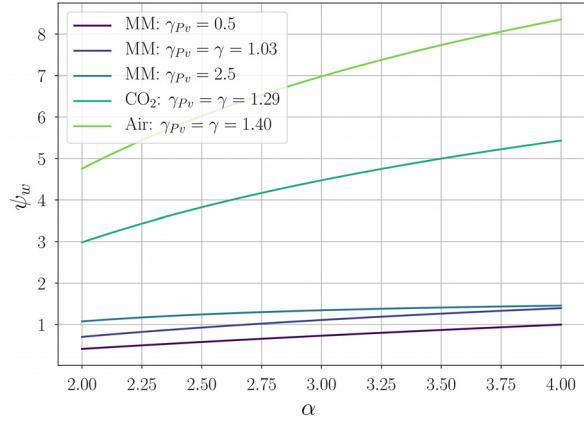


Fig. 1 Influence of molecular complexity and thermodynamic state on the normalized isentropic specific work at variable volumetric flow ratio

$$\Gamma = \frac{1}{2} \left(\gamma_{Pv} + 1 - \left. \frac{v}{\gamma_{Pv}} \frac{\partial \gamma_{Pv}}{\partial v} \right|_s \right) \quad (5)$$

and its value asymptotically approaches the specific heat capacity ratio of the fluid in the dilute gas state

$$\begin{aligned} Pv &= RT \\ \left. \frac{\partial P}{\partial v} \right|_T &= -\frac{RT}{v^2} \\ \gamma_{Pv} &= \frac{c_p}{c_v} = \gamma \end{aligned} \quad (6)$$

In turn, an explicit form of Eq. (3) valid for either ideal and non-ideal flow conditions can be obtained by substituting the heat capacity ratio with the isentropic pressure–volume exponent, under the assumption of constant γ_{Pv} . The impact of NICFD on the normalized work is displayed in Fig. 1 for siloxane MM in two non-ideal conditions, characterized by $\gamma_{Pv} > \gamma$ and $\gamma_{Pv} < \gamma$. It can be seen that non-ideal effects lead in both cases to a variation of the normalized isentropic work, ultimately affecting the stage Mach numbers and performance. Since γ_{Pv} is function of the local thermodynamic state, its average value over the expansion process can be therefore deemed a convenient parameter to quantify the impact of NICFD effects in turbomachinery. This concept is further illustrated in Fig. 2 by means of the application of a quasi-1D framework to compute isentropic expansions of siloxane MM at $\alpha=4$ in three different thermodynamic conditions, identified by the values of the reduced inlet temperature $T_r = T_{t,in}/T_c$ and pressure $P_r = P_{t,in}/P_c$, as reported in Table 2.

In the dilute gas state, whereby $\gamma_{Pv} \approx \gamma$, the evolution of flow quantities can be accurately predicted with the perfect gas law. Conversely, in the proximity of the critical point, γ_{Pv} can be either higher or lower than γ , leading to non-ideal fluid-dynamic effects, which entail significant variations of the resulting Mach number. In particular, for the same α , if $\gamma_{Pv} > \gamma$, the average Mach number along the expansion largely exceeds the value obtained in ideal gas conditions, and vice versa.

Based on these considerations, it can be argued that the best choice of the key conceptual stage design parameters may depend on the considered fluid molecule and the associated thermodynamic flow conditions. In order to investigate whether this is the case, it is more convenient to turn the CSE into a form, which explicitly includes the volumetric flow ratio α , and the isentropic pressure–volume exponent γ_{Pv} . The volumetric flow ratio $\alpha = \beta_{Pv}^{-1}$ is a more informative scaling parameter than the expansion ratio $\beta = P_{t,0}/P_3$, as it allows one to account for compressibility effects while mitigating the influence of the considered working fluid

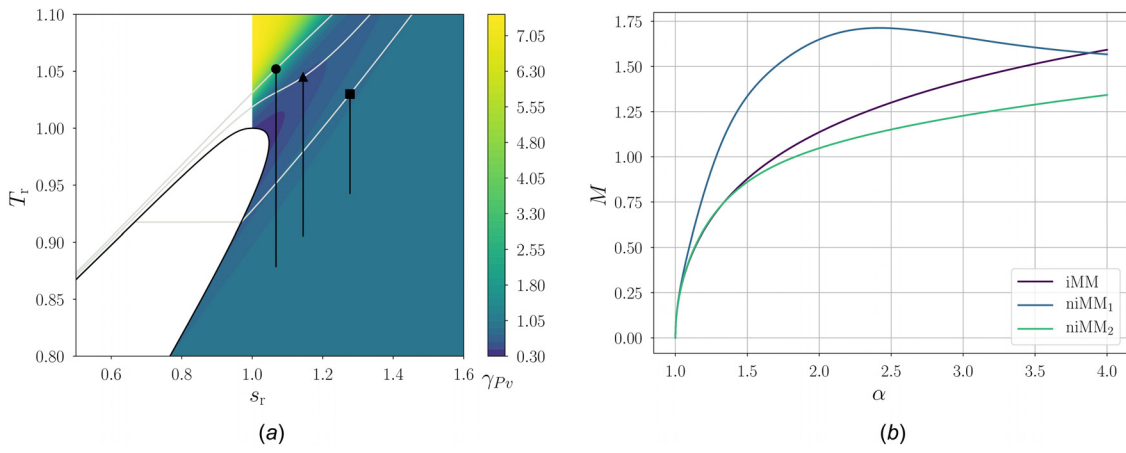


Fig. 2 Influence of the reduced inlet conditions on the Mach number profile measured along the expansion of siloxane MM at $\alpha = 4$ in a fictitious nozzle. ■ iMM; • niMM₁; ▲ niMM₂. (a) γ_{Pv} contours in the T_r - s_r thermodynamic plane and (b) Mach versus α .

Table 2 Working fluids and reduced inlet conditions analyzed in this study

Case name	Fluid	P_r	T_r
iCO ₂	CO ₂	1.0	3.0
sCO ₂	CO ₂	3.0	1.5
iMM	MM	0.5	1.03
niMM ₁	MM	2.071	1.052
niMM ₂	MM	1.3	1.045

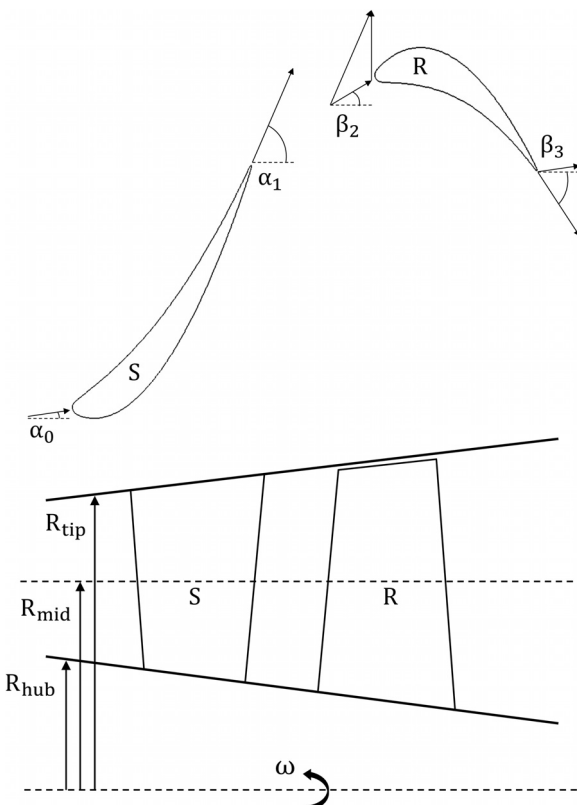


Fig. 3 Exemplary turbine stage geometry: blade-to-blade and meridional views

when operating in dilute gas state. In the light of the above, the generalized form of the CSE can be rewritten as

$$\eta = f(K_{is}, \phi, \chi^*, \alpha, \gamma_{Pv}, Re, \sigma) \quad (7)$$

In the following, Eq. (7) will be referred to as non-ideal similarity equation (NISE). Note that the loading coefficient and the degree of reaction are now normalized with the total-to-static enthalpy drop of the stage to be consistent with the definition of α . The calculation of axial turbine stage efficiency by means of the NISE is carried out according to the method described in the following.

2.2 Stage Layout. The representative turbine stage analyzed in this work is depicted in Fig. 3. The three-dimensional blade geometry is assumed to be constituted by a series of two-dimensional airfoils, characterized by negligible thickness and parabolic camber line, radially stacked according to free-vortex design. The blade spacing and stagger are given in terms of solidity $\sigma = c/s$ and axial solidity $\sigma_{ax} = c_{ax}/s$, while the annular geometry is characterized by the blade aspect ratio $AR = (H_{in} + H_{out})/2c_{ax}$ and hub-to-tip radius ratio. The gap between rotor tip and turbine casing is expressed in terms of percentage of blade height $2g/(H_{in} + H_{out})$, whereas the stator has no clearance. All turbine stages are designed at constant mean radius and constant meridional speed. The velocity triangles are univocally determined by the choice of the duty coefficients K_{is}, ϕ, χ^* , the midspan radius variation in the rotor and the stator inlet flow angle, see Eq. (8). The latter is set according to repeated stage assumption, i.e., $\alpha_0 = \alpha_3$

$$\begin{aligned} \lambda &= 2 \left(\phi_2 \tan \alpha_2 - \frac{R_{m,3}}{R_{m,2}} \phi_3 \tan \beta_3 - \left(\frac{R_{m,3}}{R_{m,2}} \right)^2 \right) \\ K_{is} &= \lambda + \phi_3^2 + \left(\phi_3 \tan \beta_3 + \frac{R_{m,3}}{R_{m,2}} \right)^2 \\ \chi^* &= \frac{1}{K_{is}} \left(1 - \left(\frac{R_{m,3}}{R_{m,2}} \right)^2 + \phi_3^2 (1 + \tan^2 \beta_3) + \right. \\ &\quad \left. - \phi_2^2 (1 + \tan^2 \alpha_2) + 2\phi_2 \tan \alpha_2 - 1 \right) \\ \beta_2 &= \arctan \left(\tan \alpha_2 - \frac{1}{\phi_2} \right) \\ \beta_3 &= \arctan \left(\tan \beta_3 + \frac{R_{m,3}}{R_{m,2}} \frac{1}{\phi_3} \right) \end{aligned} \quad (8)$$

2.3 Numerical Framework for Axial Turbine Stage Design. The numerical framework consists of a reduced-order turbine stage model schematically described in Fig. 4.

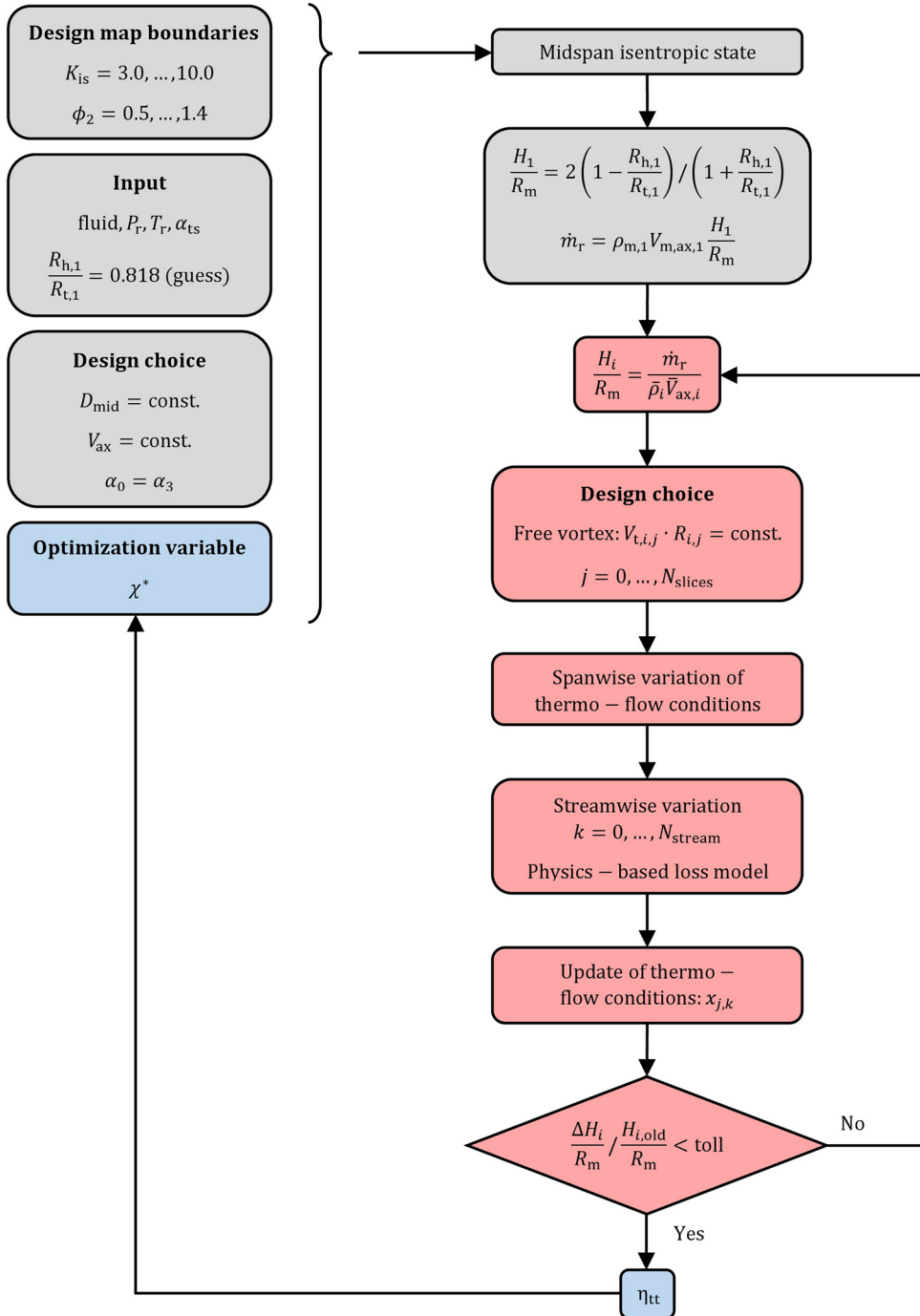


Fig. 4 Flowchart of the reduced-order turbine stage model. Initial calculations are highlighted in black, inner mass flow balance loop is highlighted in red, outer efficiency optimization loop is highlighted in blue.

The streamwise flow distribution within the blade passages is modeled assuming the simplified blade surface velocity profile depicted in Fig. 5 [13] and the spanwise evolution of flow quantities is obtained imposing free-vortex design. The two parameters ΔV and k featuring the velocity profile on the pressure and suction side of each blade section are computed by resorting to the circulation theorem and the tangential momentum balance, respectively. The latter is solved iteratively to account for compressibility effects and non-linearity introduced by the use of arbitrary thermodynamic models [14]

$$\oint \mathbf{V} \cdot d\mathbf{s} = (V_{ss} - V_{ps})c_s = \Delta V_{ts} \quad (9)$$

$$\dot{m}\Delta V_t = (P_{ps} - P_{ss})c_{ax}\bar{H} \quad (10)$$

With the purpose of providing quantitative assessment of the influence of each parameter of Eq. (7), a set of 900 stage designs is generated at varying flow and loading coefficients and the results shown in the form of efficiency maps. More specifically, upon specification of the volumetric flow ratio, reduced inlet conditions and an initial guess of the dimension of the blade channel relative to the mean radius, the model is applied to perform a stage design for each couple of ϕ_2 and K_{is} , while optimizing χ^* . The effect of Reynolds number is disregarded in this study, since the turbine stages are assumed to operate in fully turbulent regime. The geometrical characteristics of the stage are either computed

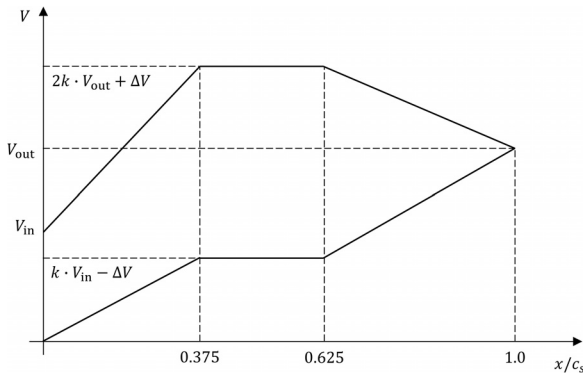


Fig. 5 Simplified velocity distribution in the blade-to-blade plane [13]

Table 3 Non-dimensional stage geometrical characteristics fixed in the reduced-order turbine stage model

Parameter	Description	Value
AR	Blade aspect ratio	3
t/s	Trailing edge to pitch ratio	0.02
g/H _{rot}	Rotor tip gap over blade height	0.01

according to best practices, i.e., optimal solidity estimated by Zweifel criterion [16] or fixed at reference values, see Table 3. The blade aspect ratio is automatically adjusted in order to attain a flare angle lower than 30 deg, even in presence of large blade height variation from inlet to outlet.

Due to its simplicity, the model is well suited to capture performance trends over a wide design space, but it must rely on loss models to account for the entropy generation in each blade passage. Traditional loss models are based on semi-empirical correlations of experimental data obtained either from cascade tests or from performance measurements of actual gas turbines. When tuned for specific applications, such correlations can provide the designer with accurate efficiency predictions. However, their accuracy becomes uncertain for performance prediction of turbine stages operating with flows highly departing from the ideal gas state. In order to capture the effect of the fluid molecule and of the thermodynamic regime on turbine efficiency, the present numerical framework is complemented with an extended version of the first-principles loss model originally reported in Refs. [12] and [13]. The models used to compute the individual loss contributions in terms of entropy generation are described in the section Loss Modeling.

3 Loss Modeling

3.1 Boundary Layer Loss. The entropy production rate due to viscous dissipation in a two-dimensional boundary layer can be estimated as [12]

$$\dot{S} = \int C_d \frac{\rho_e V_e^3}{T_e} dx \quad (11)$$

where C_d is the dimensionless dissipation coefficient

$$C_d = \frac{T_e}{\rho_e V_e^3} \frac{d}{dx} \int_0^\delta \rho V_x (s - s_e) dy \quad (12)$$

Once the velocity distribution on the blade pressure and suction side is known, the local thermodynamic state at the edge of the boundary layer can be computed by resorting to the conservation of energy and by assuming that the core flow is isentropic within the blade passage. The use of the dissipation coefficient is advantageous in presence of turbulent boundary layers, because,

differently from the friction factor, its value is weakly dependent on the state of the boundary layer. Denton [12] suggests that for conventional turbomachinery applications, where the average Re_0 is of the order of 1000 and the shape factor is in the range $1.2 < H < 2$, a reasonable approximation is to take $C_d = 0.002$. The same value is adopted in this work. Note, however, that the research documented in Ref. [18] revealed that the value of the dissipation coefficient is function of the flow regime for fluids made by simple molecules, ultimately affecting the calculated boundary layer loss.

3.2 Mixing Loss. The overall entropy production due to mixing downstream of a cascade can be estimated with a control volume analysis, applied between the throat section and a far downstream boundary, where the flow is assumed to be uniform. The conservation laws in the control volume read

$$\begin{aligned} \dot{m} &= \rho_a V_a (a - \delta^*) = \rho_{mix} V_{mix} \cos \alpha_{mix} s \\ \dot{m} V_a - \rho_a V_a^2 \theta + P_a a + P_b t \cos \alpha_a &= \dot{m} V_{mix} \cos \delta + P_{mix} s \cos \alpha_a \\ h_a + \frac{V_a^2}{2} &= h_{mix} + \frac{V_{mix}^2}{2} \end{aligned} \quad (13)$$

If the flow at the outlet section of the cascade is supersonic, the average flow conditions at the choked throat section can be computed resorting only to the conservation of energy; otherwise, the tangential momentum balance should be included in Eq. (13) to provide closure. As this work focuses on transonic turbine stages, the tangential momentum balance is disregarded from the system of equations. The base pressure P_b can be roughly correlated with the total-to-static expansion ratio of the cascade, see Ref. [19]. Due to their minor influence on the final loss estimation, in this study the boundary layer parameters are set to reference values measured in transonic cascades, i.e., $\theta/t = 0.075$, $\delta^*/\theta = 2$, as suggested in Ref. [20]. With this information, Eq. (13) can be solved to obtain the entropy rise due to mixing $\Delta s = s_{mix} - s_a$, and the deviation angle δ .

3.3 Shock Loss. The entropy generation across an oblique shock can be estimated with the Rankine–Hugoniot relations for two-dimensional flow [21], yielding

$$\begin{aligned} h_B - h_A &= \frac{1}{2} (P_B - P_A)(v_A + v_B) \\ \frac{P_B - P_A}{v_B - v_A} &= (\rho_A V_A \sin \epsilon)^2 \\ \rho_A \tan \epsilon &= \rho_B \tan(\epsilon - \delta) \\ V_A \cos \epsilon &= V_B \cos(\epsilon - \delta) \end{aligned} \quad (14)$$

where ϵ stands for the shock angle, δ is the deviation angle and A and B correspond to the pre-shock and the post-shock states, respectively. If the pre-shock state and the shock angle are known, Eq. (14) can be solved for the post-shock state, the deviation angle, and the resulting entropy rise $\Delta s = s(P_B, \rho_B) - s(P_A, \rho_A)$. In this study, the shock angle and the pre-shock state are correlated to the cascade outlet state according to the results of a set of two-dimensional RANS simulations of representative stages operating in ideal and non-ideal conditions, designed according to the method described in Sec. 5.1.

3.4 Endwall Loss. Endwall loss here includes viscous dissipation on the hub and casing boundary layers and viscous mixing of secondary flows. Due to the inherent complexity of secondary flows, a simple endwall loss model based on first principles is not available. Therefore, the improved semi-empirical correlation proposed in Ref. [22] is employed, see Appendix.

3.5 Tip-Leakage Loss. Tip-leakage loss is considered for the rotor only by assuming unshrouded blades. The entropy

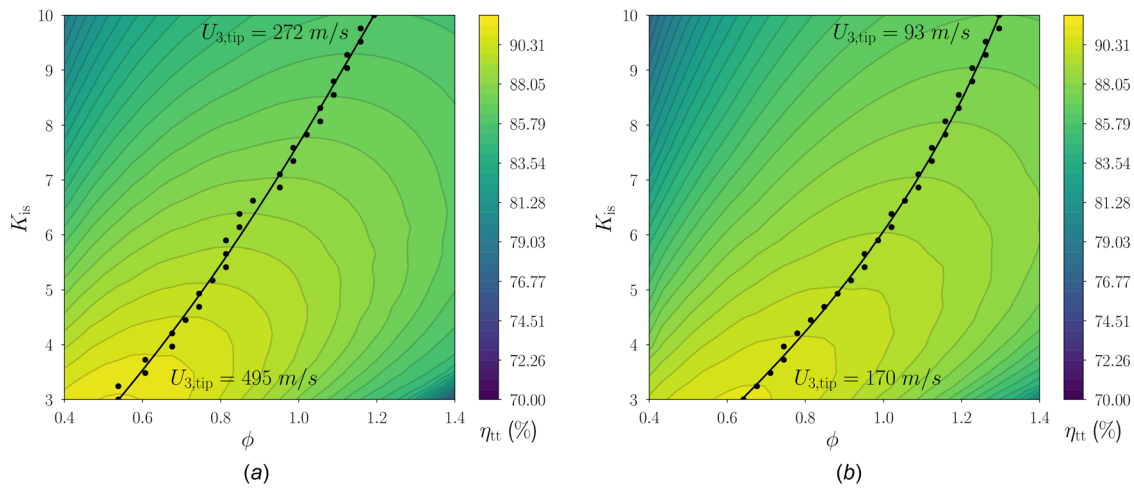


Fig. 6 Design maps at $\alpha = 4$ in dilute gas region. The dots correspond to the designs at optimal ϕ for each level of K_{is} , while the solid line represents their spline interpolation of order three. The labels show the peripheral speed at rotor tip corresponding to the lower and upper bounds of loading coefficient. (a) iCO₂ test case and (b) iMM test case.

production is calculated by means of the first-principles model proposed in Ref. [12], formulated as

$$T\Delta s = \frac{1}{\dot{m}} \int V_{ss}^2 \left(1 - \frac{V_{ps}}{V_{ss}} \right) d\dot{m}_j \quad (15)$$

where the infinitesimal leakage mass flow rate can be calculated as

$$d\dot{m}_j = C_{cu} g \sqrt{2\rho_{ps}(P_{ps} - P_{ss})} dz \quad (16)$$

and the discharge coefficient C_{cu} is equal to 0.3–0.4 for rotating cascades [12].

4 Case Studies

Best practices for design are investigated for axial turbine stages operating with siloxane MM and CO₂. The test cases are summarized in Table 2. For siloxane MM, three operating conditions are examined. For the test case labeled as *iMM*, the inlet conditions are selected such that the stage operates in the ideal gas thermodynamic region. In contrast, the conditions for the test cases denoted as *niMM* are chosen to assess the impact of strong non-ideal flow effects on loss mechanisms and optimal stage layout. In particular, for case *niMM*₁, the averaged value of γ_{pv} is higher than γ , and vice versa for case *niMM*₂. For what regards CO₂, two operating conditions are analyzed. In the same fashion as before, case *iCO₂* entails an expansion in the ideal gas regime, whereas *sCO₂* refers to a supercritical expansion, where γ_{pv} is slightly higher than γ . For all case studies, the stages feature a total-to-static volumetric flow ratio equal to 4 and a design space delimited by K_{is} in the range 3–10. The flow coefficient varies in the range 0.4–1.4 and 0.3–1.5 for the ideal and non-ideal test cases, respectively.

4.1 Influence of Fluid Molecule. The impact of the fluid molecule on turbine efficiency is evaluated by computing the design map of representative stages operating with MM and CO₂ in ideal gas conditions at $\alpha = 4$, in the form $\eta_{tt} = f(K_{is}, \phi, \gamma_{opt}^*)$. The resulting efficiency contours are shown in Fig. 6. The difference in predicted η_{tt} among the two test cases is within 1%. This efficiency difference substantially increases when computing the same design maps by fixing the total-to-static expansion ratio, thus confirming the superiority of α as scaling parameter for transonic turbine stages.

The loss breakdown of two stage designs featuring largely different values of loading coefficient, i.e., $K_{is} = 3$ and $K_{is} = 10$, and

the correspondent optimal values of flow coefficient, is depicted in Fig. 7 for both CO₂ and MM. At $K_{is} = 3$, the largest discrepancies are observed for mixing and secondary losses, which are lower for the simpler fluid molecule. Boundary layer and tip leakage losses practically coincide, whereas shock loss is higher for CO₂ due to the comparatively higher Mach numbers and the higher heat capacity ratio. Overall, the effect of mixing and secondary losses is predominant and leads to the small efficiency deficit of the stage operating with MM. At $K_{is} = 10$, the difference in Mach numbers between the two stages is close the previous case, but the average stage Mach numbers are significantly higher. In turn, compressibility effects assume primary importance, promoting an inversion of trend in mixing loss and a larger difference in shock and tip leakage losses, while boundary layer and secondary losses are virtually coincident. Altogether, at high loading coefficient, the stage operating with MM is expected to be slightly more efficient than the one operating with CO₂.

As opposed to stage efficiency, the fluid molecule has large implications in terms of peripheral speed, therefore on centrifugal loads. As discussed above, fluid made by heavy molecules like MM are characterized by comparatively lower enthalpy drops, therefore by lower tip speed for the same volumetric flow ratio over the entire design space, as displayed in Fig. 6. The values of tip peripheral speed reported for the two opposite values of K_{is} reveal that the volumetric flow ratio of axial stages operating with

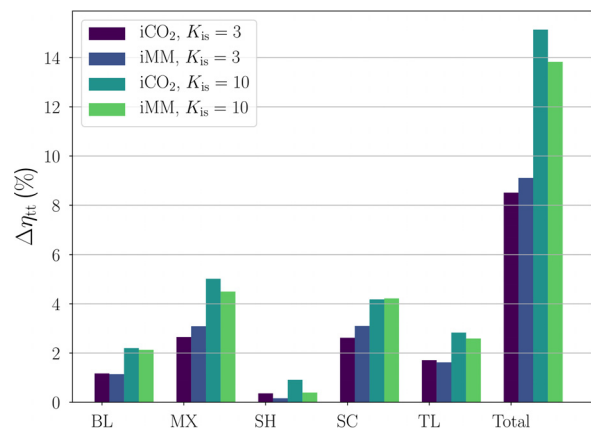


Fig. 7 Lost efficiency breakdown for test cases iMM and iCO₂ at $K_{is} = 3$ –10 and optimum flow coefficient

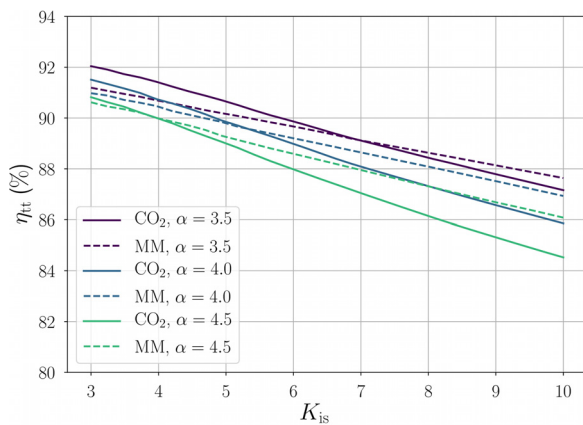


Fig. 8 Stage total-to-total efficiency at optimal flow coefficient as function of stage loading, working fluid, and volumetric flow ratio

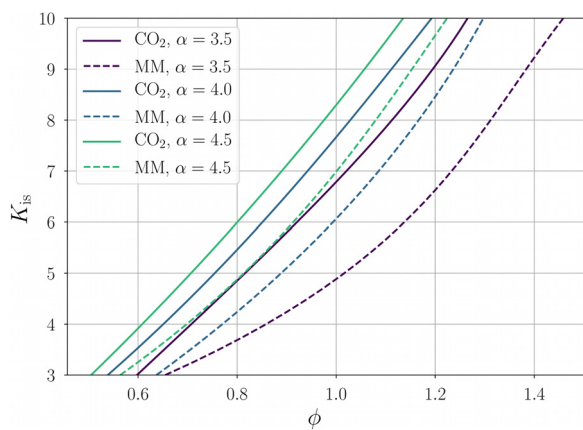


Fig. 9 Locus of optimal flow coefficient as function of stage loading, working fluid, and volumetric flow ratio

heavy fluid molecules is ideally not limited by structural reasons, even if the stage is designed at very low loading coefficient. Upper limits of α can therefore only be derived according to fluid-dynamic considerations.

4.2 Influence of Volumetric Flow Ratio. The effect of the volumetric flow ratio on the optimal choice of duty coefficients and the resulting stage efficiency is assessed by means of a parametric study conducted on test cases iCO₂ and iMM by discretely varying the α value within the range 3.5–4.5.

Figure 8 displays the efficiency trends as function of K_{is} at optimal ϕ . As expected, the efficiency decays with increasing loading coefficient and volumetric flow ratio. On average, an efficiency drop of 0.6% is found for every 0.5 increase of α at $K_{is} = 3$ for the simpler fluid molecule. The efficiency gap is nearly doubled at $K_{is} = 10$. The same trend is observed for stages operating with MM, but the efficiency drops with α are virtually halved and the performance decay with K_{is} is weaker. This result suggests that despite axial turbine stages operating with heavy fluid molecules are generally less efficient than turbines operating with simpler working fluids at low α and K_{is} ; they can provide significant performance gain at high loading and volumetric flow ratio, thus allowing to reduce the overall machine size and cost.

In addition, Fig. 9 shows the variation of the so-called Smith line, i.e., the locus of optimal design point as function of K_{is} , with the fluid molecule and the volumetric flow ratio. The curves show a clear trend: the optimal design point moves toward higher flow coefficients for increasing fluid molecular complexity,

increasing stage loading and decreasing α . In other words, for each K_{is} , the best efficiency point and the corresponding optimal stage layout become function of the volumetric flow ratio and the selected working fluid. The physical reason thereof is intimately related to the trend of shock and mixing losses. The share of both these loss sources is directly proportional to the characteristic Mach numbers of the cascades, which also directly scale with ϕ , γ , and α . Therefore, at high α , shock and mixing losses become predominant, and an attenuation of total entropy production can be only obtained by designing the stage at lower values of flow coefficient. This effect is more pronounced as the value of γ increases, namely, the simpler is the fluid molecule.

4.3 Influence of Non-Ideal Flow Effects. The impact of NICFD on axial turbine design and performance is analyzed for stages operating with siloxane MM representative of supercritical organic Rankine cycle applications, namely, the test cases labeled niMM₁ and niMM₂. The result of an additional calculation performed with CO₂ in supercritical conditions, i.e., test case sCO₂, is included in Fig. 10, but the correspondent design map and loss breakdown for the best efficiency point are omitted for brevity. The reason of that is twofold. First, γ_{pv} shows only limited deviation relative to γ along the prescribed supercritical expansion, thus leading to small variations of performance trends and optimal duty coefficients with respect to case iCO₂. Second, due to the different shape of the isentropic lines, a CO₂ expansion in the proximity of the critical point would entail excursion in the two-phase region, and the study of expansion with phase change is beyond the scope of this work.

The resulting performance maps are shown in Fig. 11. For case niMM₂, the absolute value of efficiency is significantly higher over the entire design space and the region of optimal design is shifted toward larger flow coefficients as compared to case niMM₁. The efficiency values and the Smith line for case iMM lie in between, see Fig. 6(b).

As anticipated, these trends can be predicted by analyzing the variation of γ_{pv} along the correspondent isentrope. Compared to the thermodynamic process in dilute gas conditions, where $\gamma_{pv} \approx \gamma$, for case niMM₁, the isentropic pressure-volume exponent assumes, on average, larger values, and the opposite occurs for case niMM₂. This leads to remarkable deviations in the Mach number trend along the expansion, see Fig. 2(b), ultimately affecting the share of the various loss sources, as depicted in Fig. 12. The predicted drop or gain in total-to-total efficiency is substantial. As expected, the main causes of such variation can be attributed to the significant deviations in mixing and shock-wave losses, which are intimately related to the characteristic stage Mach numbers.

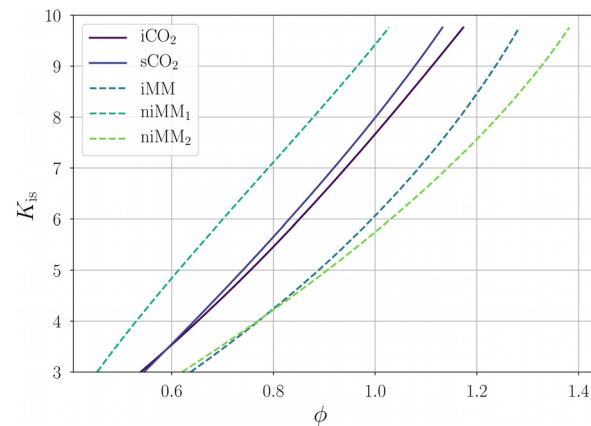


Fig. 10 Locus of optimal flow coefficient at $\alpha = 4$ as function of fluid molecular complexity and flow non-ideality

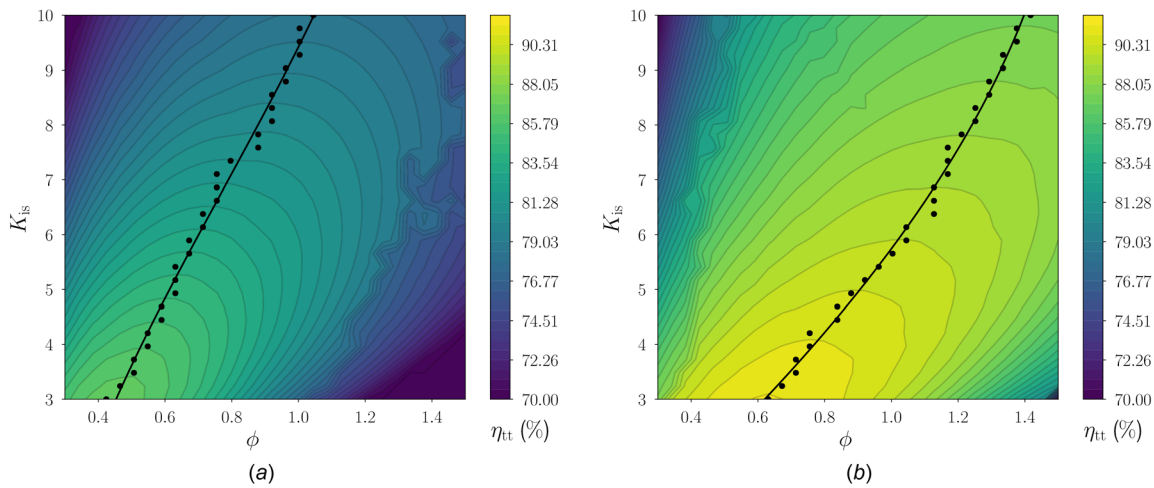


Fig. 11 Design maps at $\alpha = 4$ in NICFD conditions. The dots correspond to the designs at optimal ϕ for each level of K_{is} , while the solid line represents their spline interpolation of order three. (a) niMM₁ test case and (b) niMM₂ test case.

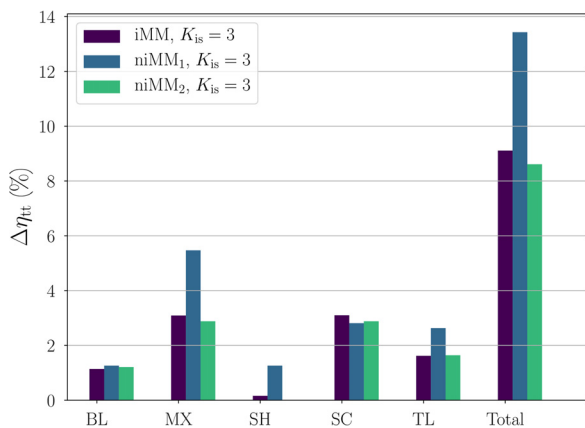


Fig. 12 Lost efficiency breakdown for best efficiency point of MM in ideal and non-ideal gas conditions

In general terms, the effect of γ_{Pv} on stage design and performance is equivalent to a change of volumetric flow ratio. In other words, an average value of γ_{Pv} higher than γ resembles an increase of α , inducing larger shock and mixing losses, thus lowering the stage efficiency and the optimal flow coefficient. Note, however that, differently from α , the departure of γ_{Pv} from γ is function of the fluid molecular complexity and thermodynamic state. In absolute terms, the significance of NICFD effects is therefore strictly fluid-dependent, with molecularly complex compounds expected to provide the highest efficiency disparities.

5 Computational Fluid Dynamics Validation

5.1 Three-dimensional Stage Geometry Reconstruction

Three-dimensional RANS and URANS simulations of the flow past turbine stages reconstructed from the output of the dimensionless turbine stage model are carried out with ANSYS-CFX [23]. The objective is to assess the capability of the first-principles loss model to provide accurate efficiency trends in both ideal and non-ideal flow conditions. Three turbine stages designed at $\alpha = 4$ and increasing blade loading, correspondent to test cases iCO₂ and iMM are selected to verify the effect of the molecular complexity. The impact of NICFD is quantified by means of two additional simulations performed on stages designed at $\alpha = 4$ and minimum blade loading, for the non-ideal operating conditions

Table 4 Dimensionless characteristics of the turbine stages selected for CFD validation

Case name	K_{is}	ϕ	χ^*
iCO ₂	3.0	0.55	0.3
iCO ₂	4.0	0.65	0.3
iCO ₂	5.0	0.8	0.3
iMM	3.0	0.55	0.3
iMM	4.0	0.75	0.3
iMM	5.0	0.85	0.3
niMM ₁	3.0	0.55	0.3
niMM ₂	3.0	0.55	0.3

corresponding to cases niMM₁ and niMM₂. The duty coefficients characterizing the selected stage layouts are summarized in Table 4.

In order to ensure full similarity between the reconstructed stage geometry and the correspondent dimensionless design, an automated design chain coupling the in-house turbine stage model, the open-source turbomachinery design system Multall [24] and the grid generator [23] is developed. The design workflow is summarized in Fig. 13. The procedure is as follows: for a given point on the performance map, the actual stage design is computed by first assigning a dimensional quantity, e.g., the mass flow rate, and then performing a mean-line design by means of the MEANGEN software, ensuring to comply with the set of nondimensional parameters provided by the in-house turbine stage model. During this process, the mass flow rate or the design point radius is iteratively adjusted to guarantee a minimum inter-row Reynolds number of the order of 3×10^6 , thus ensuring fully turbulent flow. The three-dimensional blade profiles are then generated using the STAGEN software by projecting a set of two-dimensional airfoils on the computed stream surfaces. The resulting curved profiles are then stacked along their centroids according to free vortex to be consistent with the assumptions made at preliminary design phase. The three-dimensional stage geometry is finally exported and meshed by means of a structured grid generator [23].

5.2 Numerical Setup. The boundary conditions of the CFD simulations are imposed in terms of flow direction, total pressure, and total temperature at the inlet, whereas an average static pressure is assigned at the outlet, enabling maximum local deviations within 5%. In order to reduce the computational cost, the minimum allowable number of blade passages is simulated by exploiting phase-lagged boundary conditions. $k - \omega$ SST turbulence

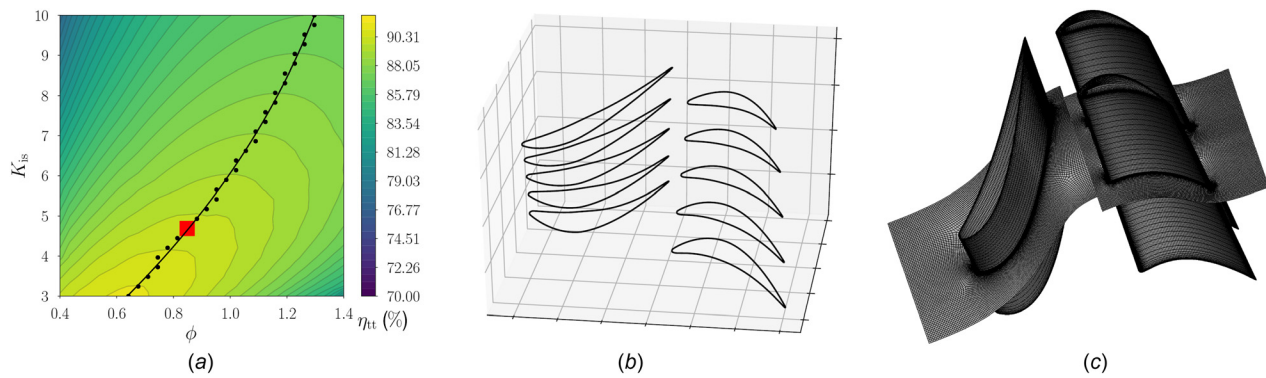


Fig. 13 Design workflow for the reconstruction of the stage geometries selected for CFD validation. (a) Target design point, (b) stage geometry reconstruction, and (c) 3D mesh.

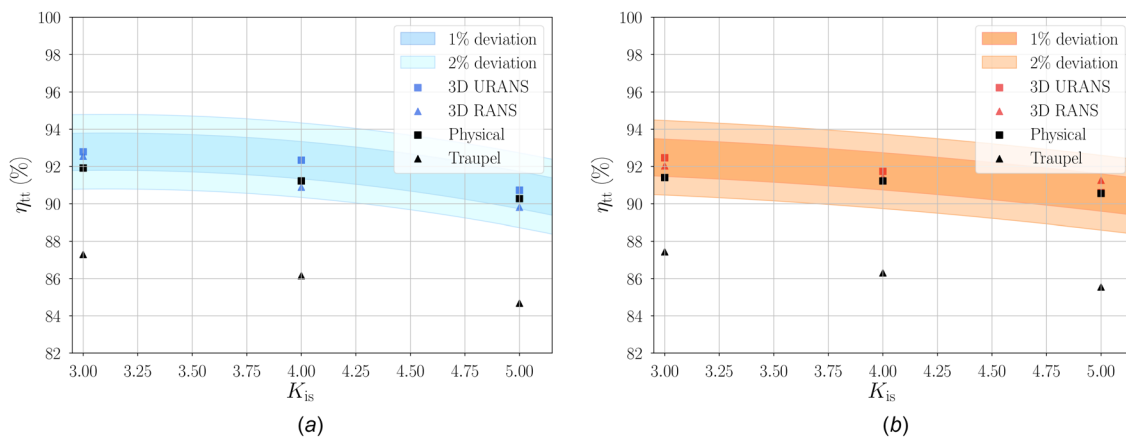


Fig. 14 Total-to-total efficiency trends of selected test cases, see Table 4, computed with the physical loss model, Traupel loss model [27], 3D RANS and URANS. (a) iCO₂ test case and (b) iMM test case.

model is employed together with adequate cell clustering near walls to guarantee $y^+ < 1$. Turbulence boundary conditions are set in terms of inlet turbulence intensity ($k = 5\%$) and eddy viscosity ratio ($\mu/\mu_t = 10$), while the turbulent Prandtl number is set to $Pr_t = 1$, in accordance with Ref. [25]. The advective and turbulent fluxes are discretized with total variation diminishing schemes [26], while a central difference scheme is adopted for discretizing the viscous fluxes. The time derivative term is discretized with a second-order backward Euler scheme. In order to speed up the evaluation of thermo-physical fluid properties, a look-up table method is employed by resorting to the reference thermodynamic library [14]. After performing a sensitivity analysis, a grid size of 4.5×10^6 cells and a thermodynamic mesh of 1×10^6 elements are set as optimal tradeoff between accuracy and computational cost. All the unsteady simulations are initialized with the results of steady-state RANS computations performed on the same stage geometries by using the mixing plane stator–rotor interface.

5.3 Results. The time-averaged total-to-total efficiency obtained by steady and unsteady CFD for the test cases iCO₂ and iMM characterized by increasing loading coefficient is displayed

Table 5 Comparison of η_{tt} predictions for stages designed at $K_{is}=3$, $\phi=0.55$ and $\chi^*=0.3$ operating with MM in ideal and non-ideal thermodynamic conditions

Case name	URANS	RANS	Physical	Traupel
iMM	92.48%	92.03%	91.41%	87.43%
niMM ₁	92.77%	89.28%	86.97%	84.76%
niMM ₂	93.98%	93.75%	91.57%	87.59%

in Fig. 14, along with the efficiency values obtained by means of the first-principles loss model as well as to the semi-empirical Traupel loss model [27]. The color bars in the charts are indicative of $\pm 1/2\%$ efficiency deviation with respect to the time-averaged values computed by 3D URANS.

Three main conclusions can be derived from these results. First, the efficiency values obtained by means of the first-principles loss model are within $\pm 1/2\%$ deviation bands for all considered test cases in ideal flow conditions, whereas the Traupel loss model

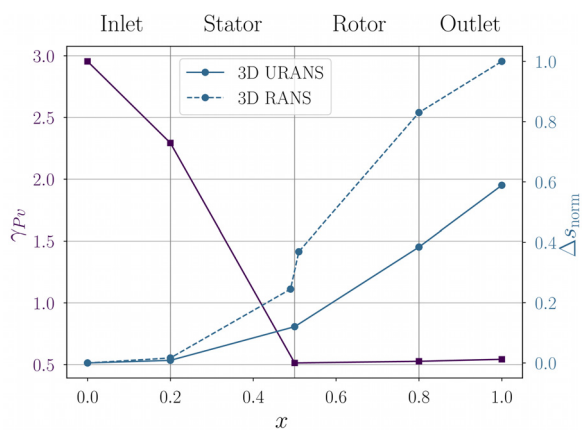


Fig. 15 Trend of the mass flow-averaged values of isentropic pressure–volume exponent and entropy generation along the normalized streamwise coordinate for test case niMM₁. The ΔS is normalized with respect to its maximum value. The URANS data are time-averaged.

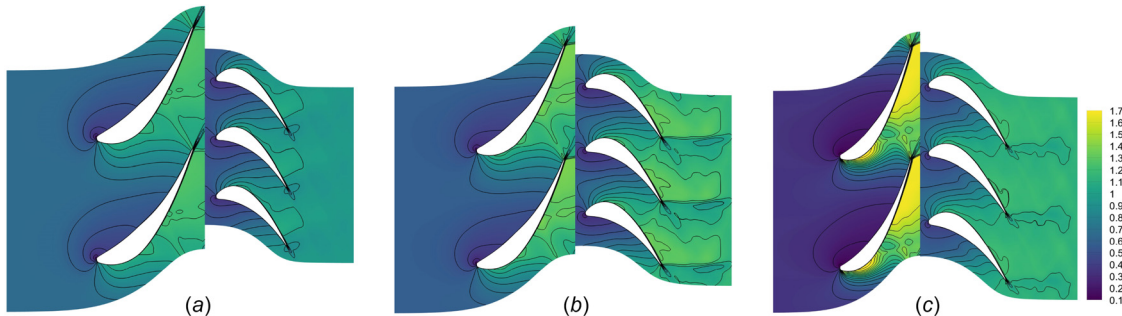


Fig. 16 Time-averaged Mach number contours at midspan computed by 3D URANS. (a) niMM₂ test case, (b) iMM test case, and (c) niMM₁ test case.

leads to a systematic underestimation of the stage performance. Both the physical and the semi-empirical loss models allow one to correctly capture the efficiency trend, with the former providing a slightly lower rate of decay as function of the blade loading. Second, the results obtained by CFD confirm that the influence of the working fluid is strongly attenuated when designing the stages at constant volumetric flow ratio in ideal gas conditions. In other words, α is verified to be a more suited scaling parameter than β to be included in the NISE. Finally, the results computed by 3D URANS corroborate the trend displayed in Fig. 8. The turbine stage operating with CO₂ is slightly more efficient than the one operating with siloxane MM at low K_{is} in ideal gas conditions. The efficiency delta progressively decreases with the stage loading, i.e., increasing the stage Mach numbers, until an inversion of trend is observed around $K_{is} = 5$ at $\alpha = 4$.

The results computed by RANS, URANS, and the turbine stage model coupled to the physical and the semi-empirical loss model for test cases iMM, niMM₁, and niMM₂ at minimum blade loading are reported in Table 5. The comparison shows that both the results of steady-state CFD and of the reduced-order model follow the same trend, namely, the total-to-total efficiency of the stage is inversely proportional to the average value of γ_{Pv} along the expansion process. While the results of 3D URANS are consistent with this tendency for test cases iMM and niMM₂, they highlight an opposite trend for case niMM₁. A thorough investigation aimed at providing an explanation to this discrepancy is out of the scope of this work. Nonetheless, some insights can be revealed by analyzing the trends of γ_{Pv} and entropy generation along the normalized streamwise coordinate, as displayed in Fig. 15. As can be observed, the γ_{Pv} value undergoes a large decrease along the expansion in the stator vanes, until a trend inversion is observed in the proximity of the stator–rotor interface. As a consequence, the Mach number reaches the maximum value at the outlet of the first row, see Fig. 16(c), where the instantaneous mixing induced by the mixing-plane interface takes place in the RANS simulations. The result thereof is an overestimation of the stator mixing loss and an alteration of the flow field in the rear part of the blade due to spurious shock waves reflection at the interface. Overall, these effects produce an underestimation of the stator efficiency and, ultimately, of the stage performance. In turn, one can infer that the performance of turbine stages featuring a non-monotonic variation of the generalized isentropic exponent can be correctly predicted only by resorting to time-resolved computational methods.

6 Conclusions

Design guidelines for axial turbine stages operating with non-ideal compressible flows have been derived using a first-principles loss model extended to arbitrary thermodynamic fluid models and the results validated through high-fidelity CFD. Based on the outcomes, the following conclusive remarks can be drawn.

- (1) A generalized similarity equation valid for turbomachinery operating with non-ideal compressible flows can be formulated by introducing the volumetric flow ratio α and the

isentropic pressure–volume exponent γ_{Pv} in place of the cascade characteristic Mach number and the perfect gas specific heat capacity ratio γ .

- (2) Both α and γ_{Pv} have a strong impact on the compressibility effects of the stage. The larger the α , the higher the mixing and shock losses; thus, the lower the stage fluid-dynamic performance and the optimal flow coefficient. An average value of γ_{Pv} larger than γ along the expansion process resembles the effects of an increase of α , and vice versa.
- (3) An increase of the volumetric flow ratio provides higher efficiency drops with loading for stages operating with fluids made by simple molecules. The net consequence is that, for complex fluids, it is possible to design efficient turbine stages even at high load coefficient and volumetric flow ratio.
- (4) The first-principles loss model is accurate within 1–2 percentage points as compared to 3D RANS for all the selected test cases. In contrast, the semi-empirical Traupel loss model [27] significantly underestimates the stage efficiency, but it provides an accurate trend prediction with loading. The results obtained with 3D URANS are in accordance with those obtained by steady-state simulations and the physical loss model, except for the case niMM₁, in which the trend of γ_{Pv} is not monotone along the expansion.

Summarizing, the optimal flow coefficient, thus the preliminary stage layout, and the stage efficiency are significantly affected by the thermodynamic regime and by the operating conditions. The reduced-order stage model based on the NISE documented in this work is suited to devise design guidelines for axial turbines operating with arbitrary working fluids and thermodynamic conditions. Future research will target the in-depth study of turbine expansion processes characterized by non-monotonic variations of γ_{Pv} by means of unsteady CFD.

Funding Data

- Aard- en Levenswetenschappen, Nederlandse Organisatie voor Wetenschappelijk Onderzoek (Grant No. 17091; Funder ID: 10.13039/501100003246).

Nomenclature

Symbols

- a = sound speed
- c = chord length
- c_{ax} = axial chord length
- c_p = specific heat capacity at constant pressure
- c_s = blade camberline length
- c_v = specific heat capacity at constant volume
- C_{cu} = discharge coefficient
- C_d = dissipation coefficient
- g = blade tip gap
- h = specific enthalpy
- H = blade height
- K_{is} = total-to-static loading coefficient

\dot{m}	= mass flow rate
M	= molecular mass
Ma	= Mach number
N	= molecular complexity
P	= pressure
R	= universal gas constant
R^*	= specific gas constant
Re	= Reynolds number
s	= specific entropy—blade pitch
T	= temperature
v	= specific volume
V	= velocity
α	= volumetric flow ratio—absolute flow angle
β	= expansion ratio—relative flow angle
γ	= heat capacity ratio—stagger angle
γ_{PV}	= isentropic pressure–volume exponent
δ	= deviation angle
δ^*	= boundary layer displacement thickness
ϵ	= shock angle
η	= efficiency
θ	= boundary layer momentum thickness
λ	= total-to-total loading coefficient
ρ	= density
σ	= stage dimensionless geometrical characteristics
χ	= total-to-total degree of reaction
χ^*	= total-to-static degree of reaction
ϕ	= flow coefficient

Subscripts

a	= throat section
A	= preshock state
b	= base pressure region
B	= post-shock state
c	= critical
e	= boundary layer edge
id	= ideal gas
in	= blade row inlet
is	= isentropic
mix	= mixed-out section
norm	= normalized
out	= blade row outlet
ps	= pressure side
r	= reduced
ss	= suction side

Abbreviations

CSE	= classical similarity equation
D6	= dodecamethylcyclohexasiloxane
MM	= hexamethyldisiloxane
NICFD	= non-ideal compressible fluid dynamics
NISE	= non-ideal similarity equation
ORC	= organic Rankine cycle
R134a	= tetrafluoroethane
sCO ₂	= supercritical carbon dioxide

Appendix A: Endwall Loss Model

$$Y = \begin{cases} \frac{0.038 + 0.41\tanh(1.2\delta^*/H)}{\sqrt{\cos \gamma} \frac{\cos \alpha_{in}}{\cos \alpha_{out}} \left(\frac{H}{C}\right)^{0.55} \left(\frac{c \cos \alpha_{out}}{c_{ax}}\right)^{0.55}} & \text{if } \frac{H}{c} \leq 2 \\ \frac{0.052 + 0.56\tanh(1.2\delta^*/H)}{\sqrt{\cos \gamma} \frac{\cos \alpha_{in}}{C} H \left(\frac{c \cos \alpha_{out}}{c_{ax}}\right)^{0.55}} & \text{if } \frac{H}{c} > 2 \end{cases} \quad (\text{A1})$$

where $Y = (P_{t,in} - P_{t,out}/P_{t,out} - P_{out})$ and $\Delta s = s(P_{t,out}, h_{t,in}) - s(P_{t,in}, h_{t,in})$.

Appendix B

The turbine stage geometries used for the CFD validation can be freely downloaded at the website link.¹

References

- [1] Wilson, D. G., 1987, "New Guidelines for the Preliminary Design and Performance Prediction of Axial-Flow Turbines," *Proc. Inst. Mech. Eng., Part A*, **201**(4), pp. 279–290.
- [2] Bertini, F., Ampelio, E., Marconcini, M., and Giovannini, M., 2013, "A Critical Numerical Review of Loss Correlation Models and Smith Diagram for Modern Low Pressure Turbine Stages," *ASME* Paper No. GT2013-94849.
- [3] Colonna, P., Casati, E., Trapp, C., Mathijssen, T., Larjola, J., Turunen-Saarela, T., and Uusitalo, A., 2015, "Organic Rankine Cycle Power Systems: From the Concept to Current Technology, Applications, and an Outlook to the Future," *ASME J. Eng. Gas Turbines Power*, **137**(10), p. 100801.
- [4] Pecnik, R., Rinaldi, E., and Colonna, P., 2012, "Computational Fluid Dynamics of a Radial Compressor Operating With Supercritical CO₂," *ASME J. Eng. Gas Turbines Power*, **134**(12), p. 122301.
- [5] Patel, A., Boersma, B. J., and Pecnik, R., 2016, "The Influence of Near-Wall Density and Viscosity Gradients on Turbulence in Channel Flows," *J. Fluid Mech.*, **809**, pp. 793–820.
- [6] Harinck, J., Guardone, A., and Colonna, P., 2009, "The Influence of Molecular Complexity on Expanding Flows of Ideal and Dense Gases," *Phys. Fluids*, **21**(8), p. 086101.
- [7] Macchi, E., and Perdichizzi, A., 1981, "Efficiency Prediction for Axial-Flow Turbines Operating With Nonconventional Fluids," *ASME J. Eng. Power*, **103**(4), pp. 718–724.
- [8] Da Lio, L., Manente, G., and Lazzaretto, A., 2014, "New Efficiency Charts for the Optimum Design of Axial Flow Turbines for Organic Rankine Cycles," *Energy*, **77**, pp. 447–459.
- [9] Da Lio, L., Manente, G., and Lazzaretto, A., 2016, "Predicting the Optimum Design of Single Stage Axial Expanders in Orc Systems: Is There a Single Efficiency Map for Different Working Fluids?," *Appl. Energy*, **167**, pp. 44–58.
- [10] Wheeler, A. P. S., and Ong, J., 2014, "A Study of the Three-Dimensional Unsteady Real-Gas Flows Within a Transonic ORC Turbine," *ASME* Paper No. GT2014-25475.
- [11] Kouremenos, D. A., and Kakatsios, X. K., 1985, "The Three Isentropic Exponents of Dry Steam," *Fortsch. Ingenieurwes. A*, **51**(4), pp. 117–122.
- [12] Denton, J. D., 1993, "The 1993 Igti Scholar Lecture: Loss Mechanisms in Turbomachines," *ASME J. Turbomach.*, **115**(4), pp. 621–656.
- [13] Greitzer, E. M., Tan, C. S., and Graf, M. B., 2007, *Internal Flow: Concepts and Applications*, Cambridge University Press, Cambridge, UK.
- [14] Lemmon, E. W., Bell, I. H., Huber, M. L., and McLinden, M. O., 2018, "NIST Standard Reference Database 23: Reference Fluid Thermodynamic and Transport Properties-REFPROP, Version 10.0," National Institute of Standards and Technology, Gaithersburg, MD, Report.
- [15] Conboy, T., Wright, S., Pasch, J., Fleming, D., Rochau, G., and Fuller, R., 2012, "Performance Characteristics of an Operating Supercritical CO₂ Brayton Cycle," *ASME J. Eng. Gas Turbines Power*, **134**(11), p. 111703.
- [16] Coull, J. D., and Hodson, H. P., 2013, "Blade Loading and Its Application in the Mean-Line Design of Low Pressure Turbines," *ASME J. Turbomach.*, **135**(2), p. 021032.
- [17] Thompson, P. A., 1971, "A Fundamental Derivative in Gas dynamics," *Phys. Fluids*, **14**(9), pp. 1843–1849.
- [18] Pini, M., and De Servi, C., 2020, "Entropy Generation in Laminar Boundary Layers of Non-Ideal Fluid Flows," *Non-Ideal Compressible Fluid Dynamics for Propulsion and Power*, F. di Mare, A. Spinelli, and M. Pini, eds., Springer, Cham, Switzerland, pp. 104–117.
- [19] Sieverding, C. H., Stanislas, M., and Snoeck, J., 1980, "The Base Pressure Problem in Transonic Turbine Cascades," *ASME J. Eng. Power*, **102**(3), pp. 711–718.
- [20] Mee, D. J., Baines, N. C., Oldfield, M. L. G., and Dickens, T. E., 1992, "An Examination of the Contributions to Loss on a Transonic Turbine Blade in Cascade," *ASME J. Turbomach.*, **114**(1), pp. 155–162.
- [21] Vimercati, D., Gori, G., and Guardone, A., 2018, "Non-Ideal Oblique Shock Waves," *J. Fluid Mech.*, **847**, pp. 266–285.
- [22] Benner, M. W., Sjolander, S. A., and Moustapha, S. H., 2006, "An Empirical Prediction Method for Secondary Losses in Turbines—Part II: A New Secondary Loss Correlation," *ASME J. Turbomach.*, **128**(2), pp. 281–291.
- [23] ANSYS, 2019, "ANSYS CFX, Release 19.3," ANSYS, Canonsburg, PA.
- [24] Denton, J. D., 2017, "Multall—An Open Source, Computational Fluid Dynamics Based, Turbomachinery Design System," *ASME J. Turbomach.*, **139**(12), p. 121001.
- [25] Otero, G. J. R., Patel, A., Diez, R. S., and Pecnik, R., 2018, "Turbulence Modelling for Flows With Strong Variations in Thermo-Physical Properties," *Int. J. Heat Fluid Flow*, **73**, pp. 114–123.
- [26] Barth, T., and Jespersen, D., 1990, "The Design and Application of Upwind Schemes on Unstructured Meshes," *AIAA* Paper No. 89-0366.
- [27] Traupel, W., 1973, *Thermische Turbomaschinen*, Springer, Berlin.

¹<https://bitbucket.org/pp-team/nicfdaxialturbines.git>